

# Lock-in incoherent differential phase contrast imaging

CHIARA BONATI,\* DAMIEN LOTERIE, TIMOTHÉ LAFOREST, AND CHRISTOPHE MOSER 

Laboratory of Applied Photonics Devices, School of Engineering, Ecole Polytechnique Fédérale de Lausanne, 1015 Lausanne, Switzerland

\*Corresponding author: chiara.bonati@epfl.ch

Received 14 October 2021; revised 10 November 2021; accepted 15 November 2021; posted 15 November 2021 (Doc. ID 445896); published 22 December 2021

We introduce a lock-in method to increase the phase contrast in incoherent differential phase contrast (DPC) imaging. This method improves the phase sensitivity by the analog removal of the background. The use of a smart pixel detector with in-pixel signal demodulation, paired with synchronized switching illumination, provides the basis of a bit-efficient approach to emulate a lock-in DPC. The experiments show an increased sensitivity by a factor of up to 8, as expected from theory, and a reduction of collected data by a factor of 70, for equivalent standard DPC measurements; single-shot sensitivity of 0.7 mrad at a frame rate of 1400 frames per second is demonstrated. This new approach may open the way for the use of incoherent phase microscopy in biological applications where extreme phase sensitivity and millisecond response time are required. © 2021 Chinese Laser Press

<https://doi.org/10.1364/PRJ.445896>

## 1. INTRODUCTION

Differential phase contrast (DPC) is a microscopy technique that has recently gained attention for its simple implementation and its ability to provide accurate quantitative phase information regarding transparent samples using incoherent light [1–7]. With the use of asymmetric, incoherent illumination, it is possible to reconstruct the phase profile of weakly scattering samples by inverting approximated linear equations [1]. Several applications have been demonstrated over the years, with particular focus on biological samples [8–12] that often satisfy the requirement of low scattering.

However, it was shown that the phase sensitivity is limited to several tens of mrad [13], which prevents applications where extreme phase sensitivity is required, such as the optical imaging of action potentials, where interferometric techniques still dominate [14–19].

Several steps can be taken to maximize contrast and improve sensitivity. For example, blocking light coming from low angles can increase the contrast by up to a factor of 2 [13]. Another approach is to average multiple frames, but this comes at the cost of speed and makes real-time recording much more data intensive: the sensitivity only improves as the square root of the number of frames.

Finally, sensitivity can be improved by increasing the power of the illumination source, as the phase image is proportional to the total light intensity [1]. On the other hand, the background is also proportional to the illumination power, and for small phase modulations the background component can saturate the detector before significant sensitivity improvement is achieved.

While detectors with larger well capacity can be used to extend the dynamic range, these usually have much larger pixels, thus sacrificing either spatial resolution or field of view.

In this paper, we explore a new approach to DPC, based on lock-in amplification to directly measure the amplitude of phase modulation, produced by alternating mirrored illuminations. Using a so-called lock-in camera (heliCam, Heliotis), we demonstrate how it is possible to obtain high-contrast, background-free, full-field DPC images. Other advantages of this technique include a reduced amount of data to be collected, rejection of out of frequency modulations, and optimized use of the dynamic range. Comparative measurements of weak phase transparent samples in standard and lock-in DPC are used to show the improvement given by the proposed technique.

## 2. THEORY

In DPC, a thin, partially transparent object is usually illuminated with partially coherent light whose angular profile  $S$  is asymmetric [1]. The light transmitted by the object is then re-focused onto a detector through an optical system with pupil  $P$ . If the object being measured is weakly scattering, it is possible to linearize the equations that govern the image formation, thus obtaining [1]

$$\tilde{I}(\vec{u}_c) = B\delta(\vec{u}_c) + H_{\text{abs}}(\vec{u}_c)\tilde{\mu}(\vec{u}_c) + H_{\text{ph}}(\vec{u}_c)\tilde{\varphi}(\vec{u}_c), \quad (1)$$

where  $\tilde{\cdot}$  represents the Fourier transform operation;  $I$  is the intensity at the detector;  $\vec{u}_c$  is the transverse spatial frequency coordinate at the detector;  $B$  is the background term;  $\delta$  is the

Dirac delta;  $H_{\text{abs}}$ ,  $H_{\text{ph}}$  are the absorption and phase transfer functions; and  $\mu$ ,  $\varphi$  are the sample's absorption and phase profile. For simplicity, we will not consider the absorption term in the following, but the theory is easily generalized.

The background term and the phase transfer function can be calculated starting from the source angular profile and pupil. In particular, if a non-aberrated setup with circular pupil is considered, it is possible to show that

$$B = \iint S(\vec{u}') |P(\vec{u}')|^2 d^2\vec{u}', \quad (2)$$

$$H_{\text{ph}}(\vec{u}_c) \propto i \left[ \iint S(\vec{u}') P^*(\vec{u}') P(-\vec{u}_c + \vec{u}') d^2\vec{u}' - \iint S(\vec{u}') P(\vec{u}') P^*(\vec{u}_c + \vec{u}') d^2\vec{u}' \right]. \quad (3)$$

The image formed at the detector is thus the sum of a background term independent of the sample, and a phase term, which is our quantity of interest.

If the source profile is modulated over time, the intensity will also change accordingly. Typically, in DPC the source profile will switch between two or more mirrored profiles. This modulation can be periodic, for example,

$$S(\vec{u}, t) = \begin{cases} S(\vec{u}) & \text{for } 0 + kT \leq t < \frac{T}{2} + kT \\ S(-\vec{u}) & \text{for } \frac{T}{2} + kT \leq t < T + kT \end{cases} \quad (4)$$

The time-dependent image would then be

$$\begin{aligned} \tilde{I}(\vec{u}_c, t) &= B\delta(\vec{u}_c) + H_{\text{ph}}(\vec{u}_c, t)\tilde{\varphi}(\vec{u}_c) \\ &= \begin{cases} B\delta(\vec{u}_c) + H_{\text{ph}}(\vec{u}_c)\tilde{\varphi}(\vec{u}_c) & \text{for } 0 + kT \leq t < \frac{T}{2} + kT \\ B\delta(\vec{u}_c) - H_{\text{ph}}(\vec{u}_c)\tilde{\varphi}(\vec{u}_c) & \text{for } \frac{T}{2} + kT \leq t < T + kT \end{cases} \end{aligned} \quad (5)$$

The quantity of interest is, in this case, the amplitude of the modulated term. In standard DPC this component is isolated from the background by recording a frame for each

illumination state, and computing the difference between the two frames, such that  $\tilde{I}_{\text{DPC}}(\vec{u}_c) = 2H_{\text{ph}}(\vec{u}_c)\tilde{\varphi}(\vec{u}_c)$ . This procedure digitally removes the background, but the single raw measurements still contain it. If the modulated term  $2H_{\text{ph}}(\vec{u}_c)\tilde{\varphi}(\vec{u}_c)$  is big enough compared to the background, this is not an issue, but if the sample is too weak, the dynamic range of the detector will not be able to accommodate at the same time a powerful background and a weak modulation. Indeed, both the phase transfer function and the background term depend on the source profile and the pupil, thus any increase of the modulated term comes with an increase of the background, which might cause saturation.

In order to circumvent this problem, it is necessary to use a scheme that directly demodulates the amplitude of  $H_{\text{ph}}(\vec{u}_c, t)\tilde{\varphi}(\vec{u}_c)$ , for example using lock-in amplification. A classic lock-in detector has a single point, so it would require a scanning confocal optical system in order to obtain a full image. Clearly, this would impact the complexity and speed of the system, which is not an ideal solution.

An alternative option is to use a detector with “smart pixels,” which incorporate special electronics to perform more advanced analog operations. One such detector is Heliotis' heliCam C3, which is a detector based on CMOS technology, and whose pixels contain signal demodulation circuitry [20–23]. The demodulation stage is based on  $I$ - $Q$  direct detection, schematically depicted in Fig. 1(c) [22]. The camera outputs the frames  $I$  and  $Q$ , which are the demodulated amplitudes of the input signal multiplied by discrete quadrature signals from the local oscillator. From these demodulated frames one can then calculate the signal amplitude and phase as

$$A = \sqrt{I^2 + Q^2}, \quad \varphi = \arctan 2(I, Q) - \frac{\pi}{4}. \quad (6)$$

This type of detector can be used to obtain DPC images according to the scheme of Fig. 1(c). Assuming that two sources of illumination are used (for example, from the left and right sides of the optical axis), these can be switched periodically over

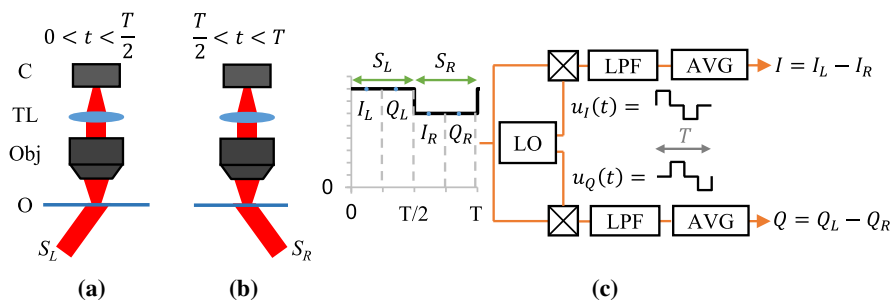


**Fig. 1.** Scheme of operation of lock-in DPC with two illuminations. (a) Simplified DPC microscope scheme during the first half period; the left source  $S_L$  illuminates the object (O), the transmitted light is collected by the objective (Obj), and an image is formed by the tube lens (TL) on the camera (C). (b) Simplified DPC scheme during the second half period, using the right source  $S_R$ . (c) Scheme of operation of a heliCam C3 pixel. The signal modulated at frequency  $1/T$  is integrated and sampled four times during each period. The local oscillator (LO) generates two discrete signals:  $u_I$  is a periodic sequence of  $[+1, 0, -1, 0]$ , and  $u_Q$  is the same signal phase shifted by  $90^\circ$ . Discrete multiplication is performed between the sampled signal and each of the two local oscillator signals. The resulting signals are then low-pass filtered (LPF) and averaged in time (AVG), giving at the output the frames  $I$  and  $Q$ , which are digitized by a 10-bit ADC. To synchronize with the DPC illumination, the two sources  $S_L$  and  $S_R$  are switched on and off alternatively over a period  $T$  equal to the demodulation period of the lock-in camera. Four samples are taken during one cycle: two while the source  $S_L$  is on ( $I_L$  and  $Q_L$ ) and two while the source  $S_R$  is on ( $I_R$  and  $Q_R$ ). If the illumination switches in phase with the local oscillator,  $I$  and  $Q$  are equal.

the period  $T$ , equal to the demodulation period, as shown in Figs. 1(a) and 1(b). During a demodulation cycle, the first two quarter period integrations sample the first illumination,  $S_L$ , while the last two sample the second illumination,  $S_R$ . After multiplication with the local oscillator signals, the output frames  $I$  and  $Q$  represent the classic DPC images. If the switching of sources is in phase with the local oscillator, the frames  $I$  and  $Q$  should be identical. For DPC, we cannot calculate the amplitude as in Eq. (6), but rather as the simple sum of  $I$  and  $Q$ , as the information about positive and negative pixel values (after subtraction) is fundamental to reconstruct a quantitative phase map of the sample. More details on the practical implementation of lock-in DPC and the relevant electronic signals within a pixel are given in Appendix A.

### A. Sensitivity

Sensitivity in DPC can be calculated from the contrast-to-noise ratio (CNR) [13,24,25]: the level of contrast that gives a CNR equal to one is considered to be the minimum amount of modulation that can be detected. If shot noise is the dominating noise source [26,27], it is possible to approximate the CNR as [13,24,28]

$$\text{CNR} \propto \frac{F^{-1}\{2H_{\text{ph}}(\vec{u}_c)\tilde{\varphi}(\vec{u}_c)\}}{\sqrt{B}}, \quad (7)$$

where  $F^{-1}$  is the inverse Fourier transform operator.

Let us now rewrite this expression in terms of source power. The source term  $S$  can be expressed as the product between the total power  $K$  and the normalized source, which depends on the direction  $\vec{u}$  of the emitted photons:

$$S(\vec{u}) = K \cdot S_{\text{norm}}(\vec{u}), \quad (8)$$

where

$$K = \iint S(\vec{u})d^2\vec{u}, \quad \iint S_{\text{norm}}(\vec{u})d^2\vec{u} = 1. \quad (9)$$

If we assume that the support of  $S$  is entirely contained in the support of the pupil  $P$ , which is normally the case in DPC, then from Eq. (2) we can see that  $B = K$ . The same normalization can be also done for  $H_{\text{ph}}$ , so that

$$H_{\text{ph}}(\vec{u}) = B \cdot H_{\text{norm}}(\vec{u}), \quad (10)$$

where  $H_{\text{norm}}$  is the phase transfer function normalized to one. By inserting Eq. (10) in Eq. (7), we obtain

$$\text{CNR} \propto \sqrt{B} \cdot F^{-1}\{2H_{\text{norm}}(\vec{u}_c)\tilde{\varphi}(\vec{u}_c)\}. \quad (11)$$

It is indeed possible to increase the CNR by simply increasing the incident power, but in standard DPC the maximum CNR is limited by saturation of the pixels.

The CNR of Eq. (11) holds equally for the lock-in scheme. In this case, the maximum CNR can be limited in three ways: (1) the source has reached its maximum power and cannot be further increased; (2) the modulation is saturating the pixels, in which case the maximum CNR is reached; (3) the background term between the two illuminations is not identical, and their difference  $B_L - B_R$  saturates the pixels. In our current implementation, this last case turned out to limit the CNR improvement the most. While the average background power can be

easily tuned, non-uniformities in the illuminations are going to be different. Expressing the non-uniformity as a fraction  $r$  of the background  $B$ , we should require that it remains below the full-scale capacity of the pixels:  $rB < W$ , where  $W$  is the well capacity. In comparison, for standard DPC, we have seen that the limit is  $B < W$ . This means that for an implementation where the non-uniformity is the main limitation, the maximum theoretical CNR ratio becomes

$$\frac{\text{CNR}_{\text{lock-in}}}{\text{CNR}_{\text{standard}}} = \frac{1}{\sqrt{r}}. \quad (12)$$

A more detailed derivation of this result is provided in Appendix B. For incoherent sources such as those in our setup, a uniformity level of 1% of the average intensity is presently state-of-the-art [29]. As a consequence, with our current implementation we can expect in practice a maximum improvement in sensitivity by an order of magnitude.

In the lock-in camera by Heliotis, we can set the demodulation period,  $T_{\text{lock-in}}$ , and the number of cycles that are averaged before a frame is obtained,  $k$ , which is a minimum of four. During this acquisition time of  $T_{\text{lock-in}} \cdot k$ , the two frames  $I$  and  $Q$  are obtained, which we sum as they are identical; thus the equivalent exposure time of DPC is given by

$$T_{\text{IQ}} = \frac{T_{\text{lock-in}} \cdot k}{2}. \quad (13)$$

In standard DPC, we collect the two images  $I_L$  and  $I_R$ , with an exposure time of  $T_{\text{LR}}$  for each. To obtain the DPC image, these two are subtracted. As shown before, both standard and lock-in DPC CNRs is governed by Eq. (11), which is also proportional to the square root of the total number of photons integrated by the detector:

$$\text{CNR} \propto \sqrt{T \cdot n}, \quad (14)$$

where  $T$  is the exposure time and  $n$  is the photon rate. If the power of the sources is maintained the same for both standard and lock-in DPC experiments, then we can expect the improvement of CNR as

$$\frac{\text{CNR}_{\text{lock-in}}}{\text{CNR}_{\text{standard}}} = \sqrt{\frac{T_{\text{IQ}}}{T_{\text{LR}}}}. \quad (15)$$

In the following, we will verify this ratio.

### B. Reconstruction

A key step of DPC is the reconstruction of a quantitative phase map of the sample. In order to do this, the DPC image is normalized by the background factor  $B$  [1], so that the result of the reconstruction is directly expressed in units of radians. Usually, the factor  $B$  is simply calculated as the sum of the two images with opposite illuminations since the phase modulation should cancel out. This is not possible in lock-in DPC, where the demodulated phase is directly obtained and the separate images  $I_L$  and  $I_R$  are not measured.

A simple way to circumvent this issue is to record a single standard DPC image, to use it as reference. The heliCam lock-in camera allows one to record images also as a standard detector. The sources are always driven at their maximum power, which means that the total exposure time in standard DPC has to be much shorter than in lock-in DPC, due to the

saturation caused by the strong background. Similar to the ratio of CNR in Eq. (15), the background ratio is equal to the exposure time ratio; thus we can write

$$B_{\text{lock-in}} = \frac{B_{\text{standard}} \cdot T_{\text{IQ}}}{T_{\text{LR}}}. \quad (16)$$

This estimated background will be used to reconstruct quantitative phase in lock-in DPC.

In this paper, the method of Tikhonov inversion [1] is used to reconstruct the phase sample from the DPC images. As often observed in the literature [1,2,4], the regularization parameter has been tuned empirically for each experiment, in order to adapt to the various CNR conditions tested [13,30].

### 3. SETUP

#### A. Microscope

The microscope DPC setup is shown in Fig. 2. It consists of a classic DPC microscope setup, with the addition of an extra 4f system to relay the pupil located inside the objective barrel. In order to control the NA of the setup, a variable aperture is located at the relayed pupil. After the aperture, a beam splitter separates the light in two paths: on the transmitted path, a tube lens forms an image of the sample at the lock-in camera; on the reflected path, a second 4f system is used to form an image of the pupil plane on a secondary camera. This image represents the illumination profile within the boundaries of the pupil and will be used to calculate the phase transfer function for phase reconstruction [13].

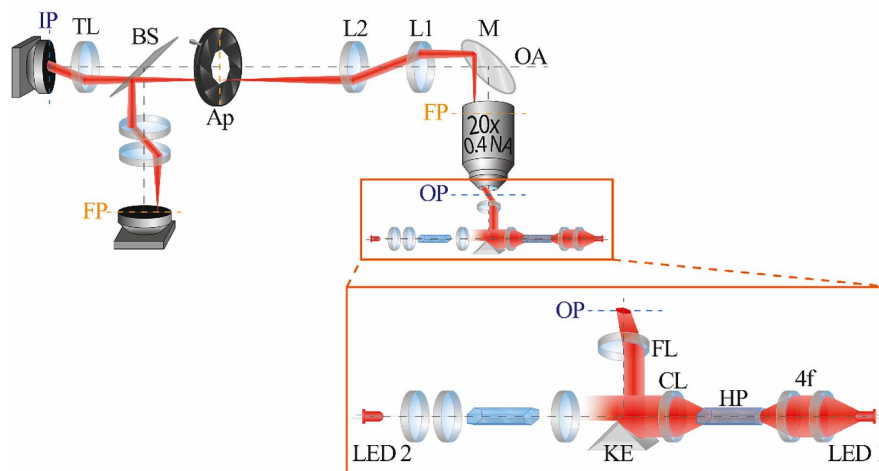


**Fig. 2.** Lock-in DPC microscope setup. The sample is located at the object plane (OP) of the objective (20×, 0.4 NA) and illuminated with red LED light (LED Engin LZ1 623 nm). The pupil (FP) of the objective is located inside the objective barrel (yellow dashed line) and is relayed with a 4f system (lenses L1 and L2, two identical 180 mm focal length lenses, with 2 in. diameter). A variable aperture (Ap) is located at the relayed pupil to adjust the system's NA to the maximum illumination angle. With a tube lens (TL, a 200 mm focal length lens, matched to the objective's specifications) an image is formed at the image plane (IP) where the lock-in camera is located. A beam splitter (BS) is used to form a second arm: there, a second 4f system forms an image of the pupil onto a standard CMOS camera. The zoomed inset shows the scheme of the illumination part of the setup. The light coming from a high-power red LED is focused with a 4f system onto the facet of a hexagonal glass pipe (HP). The light going through this glass pipe is reflected several times and gets scrambled, lighting the output facet with uniform intensity. A knife-edge mirror (KE) is placed at the back focal plane of a collimating lens (CL). This mirror has two reflecting surfaces at a 90° angle, and the edge is also reflecting. This mirror is placed such that the edge crosses the optical axis at the back focal plane. In this way the mirror acts as a Fourier filter that selects only one half of the illumination profile. A focusing lens (FL) is then placed above the KE and it makes an image of the output facet of the HP, at the OP. An identical set of elements is placed on the other side of the KE.

The heliCam C3 detector features 300 × 300 pixels with a 40 μm × 40 μm spacing. The fill factor is 50% or more thanks to a microlens array. It can demodulate signals at a frequency of up to 250 kHz, but the maximum frame rate is 3800 frames per second (fps). The frames are digitized over 10 bits.

The microscope's field of view has a size of 600 μm × 600 μm, while the pixel size limits resolution to 2 μm.

#### B. Illumination

Several strict requirements have to be met for the illumination of the lock-in DPC setup. In order to ensure the maximum field of view with unsaturated pixels, the background subtraction provided by lock-in only works if the switching illuminations have equal distributions in the object plane. Therefore, it is necessary to build a system that is able to match and align these light distributions to a high degree of accuracy. Moreover, high efficiency in light delivery is necessary, so that enough power is available to take advantage of the lock-in scheme. Finally, the NA should be as close as possible to that of the objective, in order to maximize contrast [4,13].

Considering these conditions, we opted to use two high-power red LEDs, with approximately 120° emission angle. Their emission area is obstructed by electrodes which lead to an inhomogeneous light profile, so it is not possible to directly image them onto the object plane. Among various options to even out the illumination, the use of a hexagonal light pipe was chosen (Edmund Optics, #63-080 N-BK7 Hexagonal Light Pipe). These light pipes can homogenize non-uniform light thanks to total internal reflection, so that

the output facet lights up with even intensity. The output facet can then be imaged at the object plane.

The angular distribution of this facet is still symmetric with respect to the optical axis, so it has to be filtered so that the two LEDs provide mirrored distributions that can be both focused at the same position. A convenient solution that combines the filtering and combination of illuminations is the knife-edge mirror. This is made of two mirrors at  $90^\circ$ , and the edge is also reflective (Thorlabs, MRAK25-G01). The edge is placed at the back focal plane of the collimating lens, such that it intersects the optical axis. In this way, the horizontal plane just above the knife-edge mirror will contain only half of the angular distribution of each light pipe output. A focusing lens is then placed at a focal distance from this plane, so that two similar images of the hexagonal facets are created at the object plane.

This solution is very compact, and as a consequence it is possible to use short focal length, high NA lenses, with the benefit of minimal losses and maximum NA. On the other hand, this implementation only features one axis of illumination, which can cause distortions of the phase reconstruction due to missing spatial frequencies in the direction perpendicular to the axis of illumination [1]. This issue could be solved by using custom mirrors with multiple facets, such as pyramidal for two-axis illumination. The  $I$  and  $Q$  output could then be dedicated to an axis of illumination each, rather than being identical such as in the current implementation. In this paper, we were mostly focused on contrast, and we mitigated distortions for the reconstructions in Section 4.B by making sure that none of the main edges were parallel to the illumination.

#### 4. EXPERIMENTAL RESULTS

The setup described in Fig. 2 was used to characterize the improvements given by the use of lock-in compared to standard DPC.

For each experiment, we collect images of the same sample using both DPC modalities: standard DPC, based on the difference of two images that were separately acquired, and lock-in DPC, based on in-pixel demodulation by the camera.

The lock-in camera features a so-called “intensity mode,” where two standard images at different exposure times are collected. The camera then outputs a high dynamic range image, composed of the non-saturated pixels from the two images. In order to avoid the mixing of these two images, which could introduce extra noise and make the evaluation of CNR incorrect, we maintained the average gray level around one quarter of the 10-bit range, so that only the long exposure time image is used. This means that the exposure time could be increased by a factor of 4, improving the CNR by a factor of 2, according to Eq. (14). Since we are interested in comparing the best result of lock-in DPC with the best result of standard DPC, we will take these factors into account in the following results.

Background images in the absence of a sample are also collected in order to remove unwanted illumination structures, which are particularly intense in lock-in DPC due to the strong amplification. The power of the LEDs is maintained equal during all measurements. This means that the exposure time for standard DPC has to be much shorter due to saturation.

The USAF target samples used in these experiments were fabricated by photolithography of fused silica wafers with varying etching times, in order to obtain different heights and, as a consequence, different phase values. The nominal height was calculated based on the calibrated etching rate, and later verified via atomic force microscopy measurements.

##### A. Sensitivity

The first set of measurements concerns the improvement of sensitivity that lock-in DPC allows to achieve. A qualitative comparison is shown in Fig. 3, for a USAF target whose phase difference is approximately 19 mrad. In particular, Figs. 3(a) and 3(b) show a region of interest for standard and lock-in DPC, respectively. For the lock-in image, the duration of one cycle is set to be approximately  $140 \mu\text{s}$ , and four cycles are averaged by the camera before transmitting the digitized measurement to the computer. From Eq. (13), the effective exposure time is  $280 \mu\text{s}$ . The sum  $I + Q$  is shown in Fig. 3(b), after background subtraction.

The standard DPC image is obtained by subtracting the images  $I_L$  and  $I_R$ , obtained with left-side and right-side illumination, respectively. Each image is recorded over  $1 \mu\text{s}$ , and

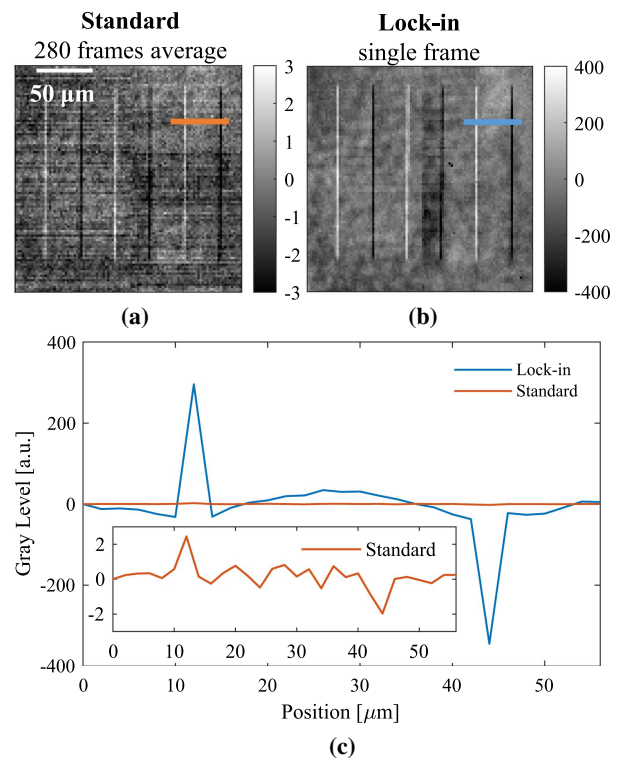


**Fig. 3.** Comparison of standard and lock-in DPC images of a 19 mrad USAF target. (a) Region of interest (ROI) of the USAF target measured in standard DPC, after background subtraction and averaging of 280 frames of  $1 \mu\text{s}$  exposure each. (b) ROI of the USAF target measured in lock-in DPC, over a total exposure time of  $280 \mu\text{s}$ , after background subtraction. This image is the sum of the two quadrature images  $I$ ,  $Q$ . (c) Comparison of the cross section of the right-most structure, in lock-in and standard DPC. The blue cross section refers to the lock-in measurement, while the orange cross section refers to a single standard measurement. The inset shows the same cross section for standard DPC, but with a zoomed scale.

Fig. 3(a) shows the average of 280 DPC images, which is approximately equivalent to the amount of integrated light in lock-in DPC.

The cross section of the USAF target obtained in the two cases is shown in Fig. 3(c), without averaging of the standard DPC case. It is possible to appreciate that, while the shape of the cross section is very similar, the intensity of the positive and negative peaks in lock-in DPC is encoded over approximately 2 orders of magnitude more than those of standard DPC. Moreover, having been able to integrate significantly more light, the relative variation of the gray level between the pixels, caused by noise, is greatly reduced in the lock-in measurement. For an equal amount of collected data, that is  $I$  and  $Q$  in lock-in, and  $I_L$  and  $I_R$  in standard DPC, it is possible to observe a much better contrast and reduced noise in the first case.

In order to analyze the improvement of contrast in a more quantitative way, we measured the CNR of several USAF samples, with varying phase values, in both DPC techniques. The CNR was calculated as the ratio between the amplitude of the cross section [maximum minus minimum, as seen in Fig. 3(c)], and the standard deviation of a featureless area [31,32].

The ratio of exposure time was again 280. The exposure time chosen for the lock-in DPC was such that some of the peripheral pixels were saturated, and thus we consider this to be the maximum amount of photons that can be integrated before significant distortion. In the standard case, the average gray level reached only one quarter of the full dynamic range, for the reasons explained previously. In order to compare the maximum CNR of both techniques, we corrected the exposure time ratio by a factor of 4, giving 70, and we multiplied all the CNR values of standard DPC by a factor of 2. The results of these measurements are given in Fig. 4(a): it is possible to observe how the CNRs for the lock-in technique are consistently greater than those of standard DPC. In particular, for the smallest sample that we used, at 5 mrad, the CNR of the standard DPC is around 0.82, which means it is already below sensitivity. On the other hand, for the lock-in case, the CNR is around 7.2, which means that the sensitivity limit would be reached around 0.7 mrad.

This is approximately a factor of 8 improvement, which is expected given the exposure time ratio of 70, using Eq. (15). Indeed, Fig. 4(b) shows the experimental ratio of CNR, plotted

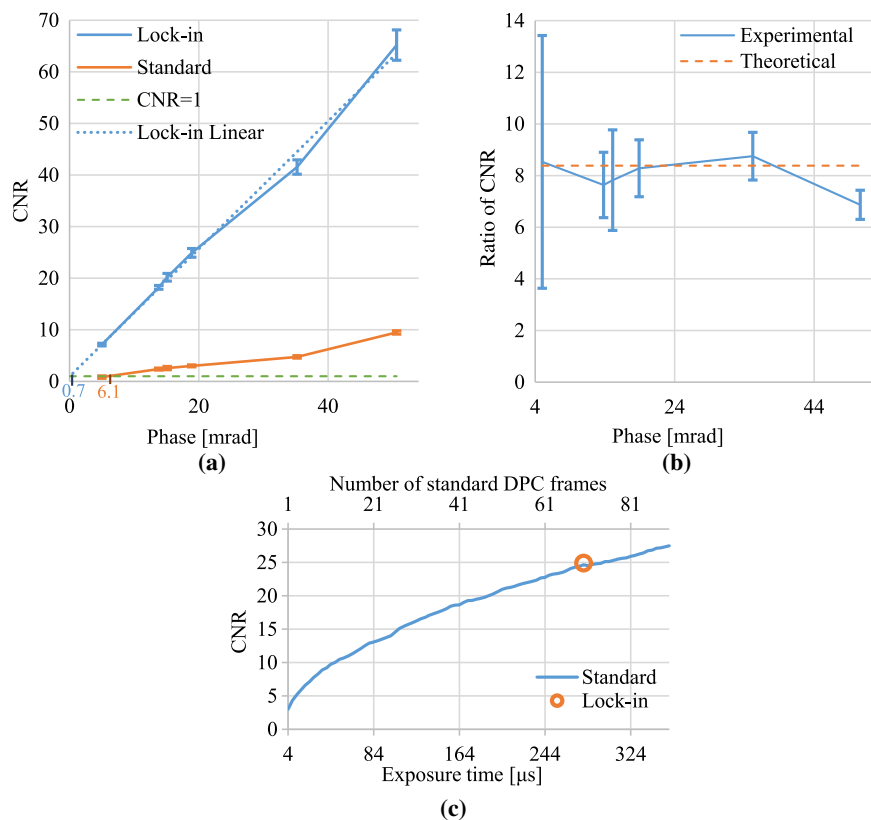


**Fig. 4.** (a) CNR, measured as the ratio of maximum and minimum peak of the cross section and the standard deviation of a featureless area, is calculated for several samples and plotted against their phase, for both lock-in and standard DPC, in blue and orange, respectively. The CNR of the standard DPC measurements has been multiplied by 2 to take into account the possibility to increase the exposure time without saturating the 10-bit detector. The error bar is obtained over 100 measurements. The green dashed line represents the sensitivity limit at  $\text{CNR} = 1$ , while the blue dotted line is the extrapolated linear trend of the CNR in lock-in DPC. According to this extrapolation, on the horizontal axis the phase sensitivities of lock-in DPC and standard DPC are shown, in blue and orange, respectively. (b) The ratio of CNR between lock-in and standard DPC is plotted against the phase of several USAF targets. This ratio should be constant, at 8.36, since the ratio of exposure time is 70, considering an extra factor of 4 for the standard measurement exposure time to reach the best-case scenario. The error bars are obtained over 100 measurements. (c) CNR for increasing number of averaged standard DPC frames, compared to a single lock-in acquisition. The top horizontal axis shows how many frames are averaged, while the bottom horizontal axis shows how much time is required in total.

for all the samples we tested, compared with the theoretical value: the experimental ratio of CNR oscillates around this value. Two of the experimental points require further explanations. The error bar for the first phase value is significantly bigger than the other ones: this is because the amplitude of the cross section in standard DPC suffered from great uncertainty due to its being below sensitivity. This error is then propagated to the ratio of CNR. The last experimental point is further from the theoretical values compared to the other cases. It is possible that the amplitude of the cross section in lock-in DPC is in fact underestimated in this case, as the modulation given by this sample was very close to saturation. Saturation of the lock-in DPC image would explain a CNR value lower than expected.

As we have shown theoretically and experimentally, for an equal amount of collected data, the CNR of lock-in DPC will be greater than that of standard DPC by a factor equal to the square root of the exposure time ratio. On the other hand, it is still possible to reach the same CNR, by averaging enough frames to reach an equivalent total exposure time, as shown in Fig. 4(c). In this experiment, we collected multiple identical frames in standard DPC, and calculated the CNR of an increasing number of averaged frames. The curve of CNR displays the classic  $\sqrt{N}$  behavior, where  $N$  is the number of samples, in the case frames. The orange circle marks the CNR value and exposure time of the lock-in case. Indeed, when 70 standard frames are averaged, reaching the same total exposure time, the CNR is very similar.

## B. Reconstruction

A key feature of DPC is the possibility of reconstructing quantitative phase information about the sample. As explained in Section 2.B, in order to do this, the DPC image has to be normalized by the background  $B$ . While this value is not known in a lock-in measurement, we described a work-around, by using the standard DPC background and multiplying it by the ratio of exposure time. As an example, we measured the phase of a reconstructed USAF target, in both standard and lock-in DPC, and the result is shown in Fig. 5. In this experiment, we reconstructed a 50.6 mrad sample. In Fig. 5(a), the reconstruction is based on a single standard DPC image, over an 8  $\mu\text{s}$  exposure. In Fig. 5(b), instead, 58 standard DPC frames were averaged, equaling the 464  $\mu\text{s}$  exposure of the lock-in DPC reconstruction of Fig. 5(c). Indeed, it is possible to see how in the first image, it is difficult to recognize the shape of the target, due to the amount of noise that has been transferred to the reconstructed phase. By averaging enough frames, it is possible to obtain a similar reconstruction quality as in lock-in. From a quantitative point of view, Fig. 5(d) shows the comparison of the cross sections from reconstructions in Figs. 5(b) and 5(c), highlighting the correct quantitative result of reconstruction for our lock-in DPC measurement, using the standard background.

In Fig. 6, we show another interesting feature of lock-in DPC, which is the possibility of modulating contrast by changing the exposure time, without the need to acquire more frames. In particular, Fig. 6(a) shows the phase reconstruction

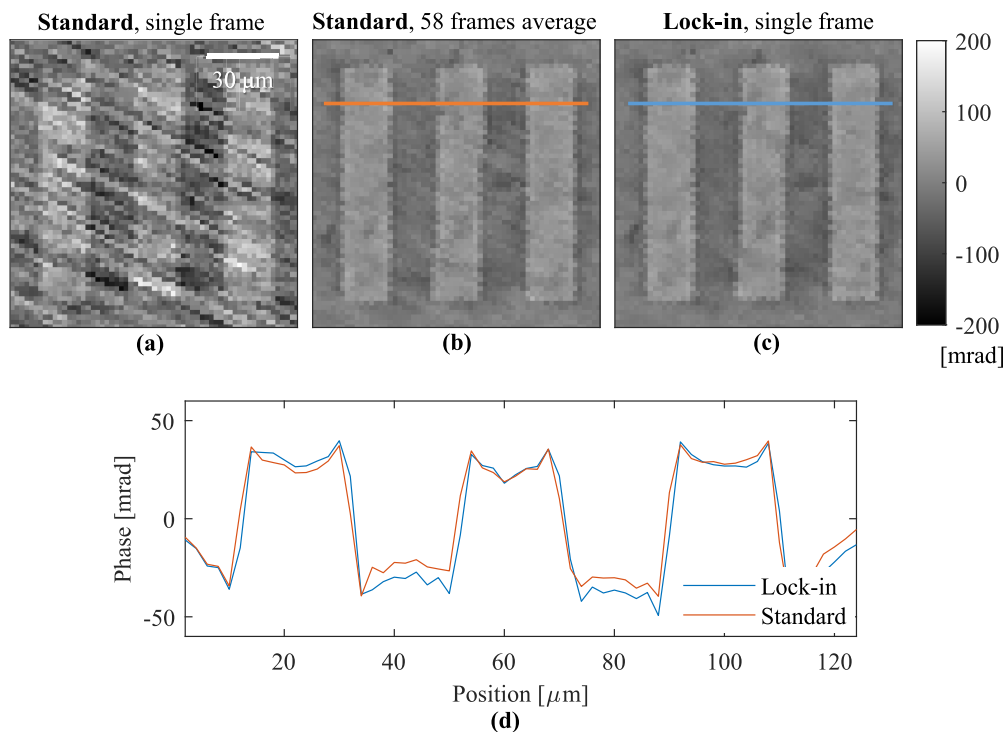


**Fig. 5.** Reconstructed phase of a 50.6 mrad USAF target. The target was placed with an angle of  $25^\circ$  with respect to the direction of illumination, so that none of the edges were parallel to it. As a consequence, no distortion is caused by the missing frequencies. The ROI is rotated here to show straight rectangles. (a) Reconstructed phase from a single 8  $\mu\text{s}$  exposure standard DPC image. (b) Reconstructed phase from 58 averaged standard DPC frames. (c) Reconstructed phase from a single 464  $\mu\text{s}$  lock-in measurement. (d) Comparison of the cross sections indicated in (b) and (c) with the orange and blue lines.

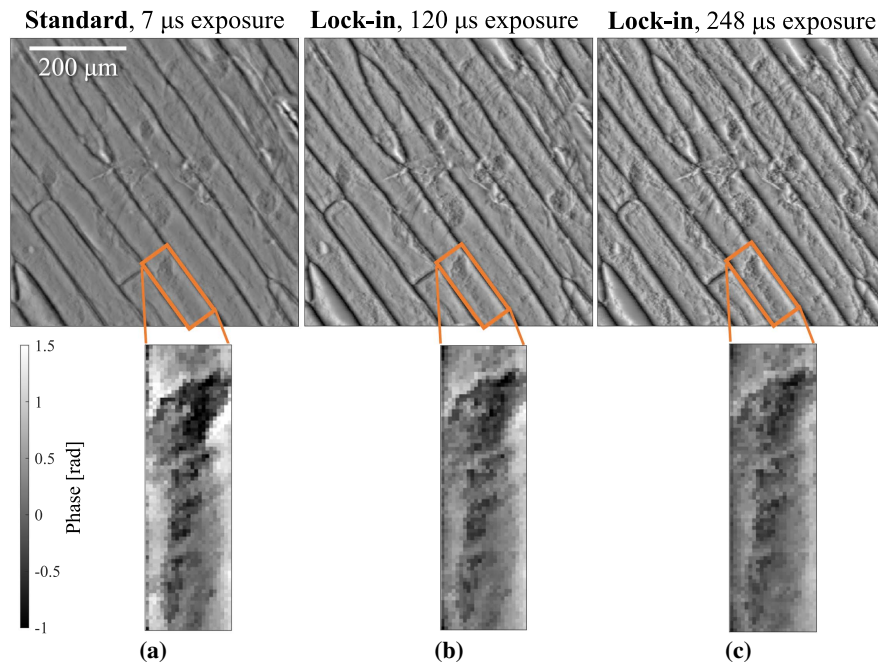


**Fig. 6.** Phase reconstruction of onion epidermal cells. (a) Reconstruction from a single, 7  $\mu\text{s}$  exposure, standard DPC image. (b) Reconstruction from a single, 120  $\mu\text{s}$  exposure, lock-in DPC image. (c) Reconstruction from a single, 248  $\mu\text{s}$  exposure, lock-in DPC image. Second row: zoom from the areas indicated in the orange squares.

from a single 7  $\mu\text{s}$  exposure standard DPC image, compared with a single lock-in exposure of 120  $\mu\text{s}$  in Fig. 6(b) and 248  $\mu\text{s}$  in Fig. 6(c). The zoomed-in areas show how some low-phase features become more nuanced using lock-in. In both Figs. 6(b) and 6(c), just a single image was collected. The zoomed-in sections are all scaled to the color bar on the left, showing that the normalization procedure allows us to retrieve the same quantitative phase as in standard DPC. As demonstrated previously, it would still be possible to obtain similar results in standard DPC, but this would require acquiring 17 images to reach the contrast of Fig. 6(b) and 35 images to reach that of Fig. 6(c), with the disadvantages that come with a more data intensive measurement, as explained in Section 4.A.

## 5. DISCUSSION AND CONCLUSION

In this paper, we have described a new approach to DPC, which takes advantage of periodic modulation of illumination to automatically extract the DPC information without encoding the background. As a consequence, longer exposure times are possible without saturation of the pixels, which allows increasing the CNR by almost an order of magnitude, in a single shot. In particular, we demonstrated an improvement by a factor of up to 8.3 of CNR for single exposures, which means that around 70 frames are needed in standard DPC to reach the image quality of lock-in DPC.

While similar sensitivities are reachable in standard DPC, it is necessary to average tens of frames, which drastically increases the bit rate of the stream from camera to computer or reduces the duration of recording for cameras with onboard memory. The power of lock-in DPC stands in being able to

reach such sensitivity in a single frame, drastically reducing the data- and time-intensiveness of the technique. For example, for a time lapse recording at 1400 frames per second, with a  $300 \times 300$  pixels detector and a 10-bit depth, we obtain a 1.26 Gbit/s rate in lock-in DPC and 88.2 Gbit/s with standard DPC for equal CNR. Current camera interface technologies can reach few tens of Gbit/s speed, such as multichannel CoaXPress, so reaching the same sensitivity as lock-in DPC at the same speed would not be possible. The current heliCam model, like most high-speed cameras, is actually equipped with an onboard memory, which dictates the maximum total recording time before images have to be downloaded to the computer. Considering, for example, an 8 GB memory, in lock-in DPC it is possible to record up to 50.79 s, compared to only 0.72 s in standard DPC. This example is summarized in Table 1.

This analysis shows that, when resorting to averaging multiple frames to obtain the same sensitivity as in lock-in DPC, the result will still be inferior: with direct computer transfer the frame rate will be lower, and with onboard memory the total recording time will be drastically reduced. Both these choices are undesirable for real-time biological imaging.

**Table 1.** Example of Bit Rate and Recording Time at 1400 Frames per Second

	Standard DPC	Lock-In DPC
Bit rate	88.2 Gbit/s	1.26 Gbit/s
Recording time for 8 GB memory	0.72 s	50.79 s
Recording time for 16 GB memory	1.45 s	101.58 s

Currently, these results are limited by the non-uniformity of the illumination, which could be improved with better illumination setups or by actively matching the sources, for example, using a spatial light modulator. If better illumination is achieved, even longer exposure time can be sustained, further increasing the single-shot sensitivity.

Another limit of this technique is the resolution and field of view given by currently available lock-in cameras. The in-pixel demodulation circuit requires a certain amount of space, giving a pixel size of  $40 \mu\text{m} \times 40 \mu\text{m}$  and a total detector size of  $300 \times 300$  pixels. On the other hand, this technical limitation may be overcome in the future.

Moreover, other types of applications can be foreseen for this type of imaging, which can be applied in any situation where weak modulations over strong backgrounds have to be measured. For example, the sample response to illuminations of different polarization or wavelength may be analyzed to map morphological or chemical structures within the sample.

Overall, this approach may enable easier measurement of weak phase details or dynamic phenomena, such as in biological samples, where only interferometric techniques were applied until now [14–16]: for example, Ling *et al.* [15] successfully imaged action potentials in an interferometric system with 0.3 mrad sensitivity and 1000 fps. In our experiments, we have obtained a sensitivity of 0.7 mrad over a 1400 fps frame rate, which comes quite close to the requirements of action potential imaging, while removing issues associated with the use of coherent sources, such as speckle noise. This performance is currently unparalleled in any incoherent phase contrast imaging system.

While further improvement of the illumination setup and spatial resolution may be necessary, future applications of this technique will be of interest for several scenarios in biology.

### APPENDIX A: LOCK-IN OPERATION FOR DPC

In this section, we provide a more detailed explanation of how the lock-in camera can be used for DPC.

Let us assume that the sample under observation is the simulated phase sample depicted in Fig. 7(a). When the sample is illuminated with the left source in Fig. 1(a), the image at the camera would be as shown in Fig. 7(b). Under right source illumination, the resulting image would be as in Fig. 7(c). We can focus on the intensity received by the pixels on the left-most rectangle edge, highlighted in the orange circle in Figs. 7(b) and 7(c). If the light sources are switched over a period  $T$ , tracking the intensity received by the pixels of interest would give a plot such as shown on the left in Fig. 7(d). This is the input light modulation at the detector.

The lock-in camera integrates four samples from the input signals, each with a duration of one quarter of the local oscillator period. The key to performing lock-in DPC is to set the light switching period to be equal to the local oscillator period, and to make sure that they are synchronized in phase. In this way, the first two samples ( $I_L$  and  $Q_L$ ) are obtained during the left illumination, while the last two samples ( $I_R$  and  $Q_R$ ) are obtained during the right illumination. Moreover,  $I_L$  and  $Q_L$  are equal, as well as  $I_R$  and  $Q_R$ .

The local oscillator generates two periodic signals with period  $T$ ,  $u_I$  and  $u_Q$ , which are a sequence of  $[+1, 0, -1, 0]$ , and are shifted in phase by  $90^\circ$  with respect to each other. These

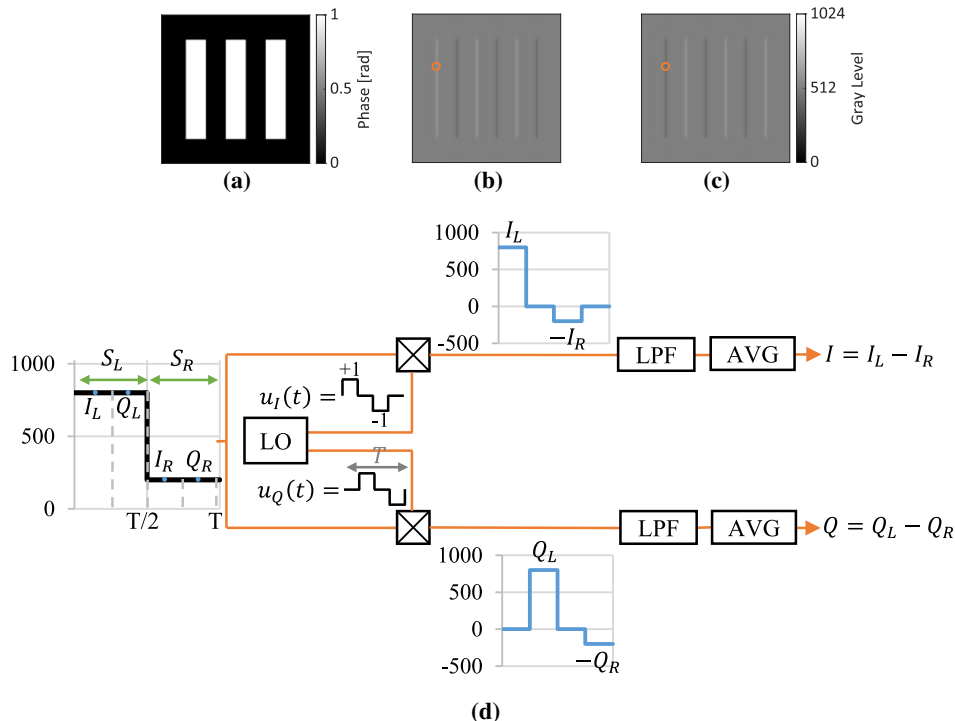


**Fig. 7.** (a) Simulated phase sample; (b) simulated image formed under left-illumination conditions ( $S_L$ ); (c) simulated image formed under right-illumination condition ( $S_R$ ); (d) scheme of operation of lock-in DPC, when the synchronization in frequency and phase is correctly done.

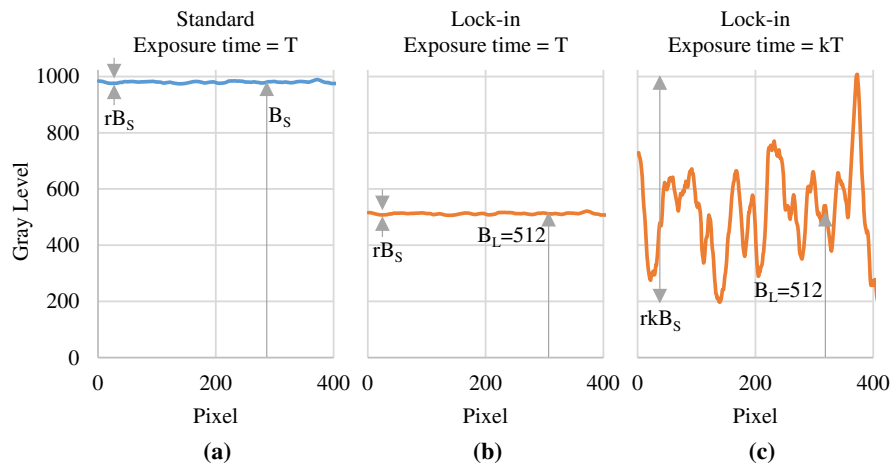


**Fig. 8.** (a) Simulated pixel values along a cross section, for standard DPC image recorded over an exposure time  $T$ .  $B_S$  indicates the background value, close to the limit of 1024 in the case of a 10-bit detector;  $rB_S$  indicates the amplitude of the background non-uniformity. (b) Simulated pixel values along the same cross section, for a lock-in DPC image recorded over an exposure time  $T$ .  $B_L$  indicates the background value, which is approximately 512 if the left–right illuminations are tuned to have the same average power; the non-uniformity is still  $rB_S$ . (c) Simulated pixel values along the same cross section, for a lock-in DPC image recorded over an exposure time  $k$  times of before. The background is still 512 assuming well-tuned illuminations, but the non-uniformity is now increased by the same factor  $k$  as the exposure time.

two periodic signals are multiplied with the four input samples, giving the two quadrature signals in blue in Fig. 7(d). The last stages are low-pass filtering and averaging, after which two single frames,  $I$  and  $Q$ , are output by the camera.

Unlike applications such as optical coherence tomography, in this case the only quantity of interest is the amplitude of the signal. Moreover, if timing of the illumination has been done correctly,  $I$  and  $Q$  are identical, and from Eq. (6) the phase between them is always zero. Since we also need to preserve information on the positivity and negativity of pixel values with respect to the background, which would be lost with Eq. (6), we calculate the lock-in DPC image simply as the sum of  $I$  and  $Q$ .

## APPENDIX B: CNR IMPROVEMENT LIMIT

As briefly introduced in Section 2.A, the CNR improvement given by the lock-in method compared to the standard method, is currently limited by the background non-uniformity.

We define the single-shot CNR improvement as the ratio between the maximum lock-in CNR and the maximum standard CNR, for the same sample. Let us first write the CNR limit for the standard method, using Eq. (11). The most simple way to improve the CNR is by increasing the background intensity  $B$ ; this is of course limited by the well capacity of a pixel,  $W$ , since higher intensities would saturate the image making any analysis impossible. This means that the theoretical maximum standard CNR is

$$\text{CNR}_{S,\max} \propto \sqrt{W} \cdot F^{-1}\{2H_{\text{norm}}(\vec{u}_c)\tilde{\varphi}(\vec{u}_c)\}. \quad (\text{B1})$$

Of course, this is a limit case, since non-uniformity and phase structures may increase the intensity in some pixels at the saturation level. We will express the amplitude of the background non-uniformity as a percentage  $r$  of the background  $B_S$ , as shown in Fig. 8(a).

In the lock-in case, for the same exposure time  $T$ , the cross section would look as in Fig. 8(b), where the background  $B_L$  is approximately 512: if the left and right illuminations are properly tuned to have the same average intensities, there would be no modulation over time, and the camera maps this to the mid-level of the scale. The non-uniformity here is still  $rB_S$ . In this case though, none of the pixels are close to saturation, so we can safely increase the exposure time, thus improving the CNR. If we increase the exposure time by a factor  $k$ , the non-uniformity also increases by the same factor, as depicted in Fig. 8(c). Clearly in this situation, the limit is reached when the amplitude of non-uniformity equals the maximum gray level  $W$ , so we can write

$$\begin{aligned} k_{\max} r B_S &= W \Rightarrow k_{\max} = \frac{W}{r B_S}, \\ \text{CNR}_{L,\max} &\propto \sqrt{k_{\max} B_S} \cdot F^{-1}\{2H_{\text{norm}}(\vec{u}_c)\tilde{\varphi}(\vec{u}_c)\} \\ &= \sqrt{\frac{W}{r}} \cdot F^{-1}\{2H_{\text{norm}}(\vec{u}_c)\tilde{\varphi}(\vec{u}_c)\}. \end{aligned} \quad (\text{B2})$$

As a consequence, the maximum CNR improvement is given as

$$\frac{\text{CNR}_{L,\max}}{\text{CNR}_{S,\max}} = \sqrt{\frac{1}{r}}. \quad (\text{B3})$$

**Disclosures.** The authors declare no conflicts of interest.

**Data Availability.** Lock-in and standard DPC images will be made available on Zenodo upon publication.

## REFERENCES

1. L. Tian and L. Waller, "Quantitative differential phase contrast imaging in an LED array microscope," *Opt. Express* **23**, 11394–11403 (2015).

2. Z. F. Phillips, M. Chen, and L. Waller, "Single-shot quantitative phase microscopy with color-multiplexed differential phase contrast (cDPC)," *PLoS ONE* **12**, e0171228 (2017).
3. Y.-H. Chuang, Y.-Z. Lin, S. Vyas, Y.-Y. Huang, J. A. Yeh, and Y. Luo, "Multi-wavelength quantitative differential phase contrast imaging by radially asymmetric illumination," *Opt. Lett.* **44**, 4542–4545 (2019).
4. Y. Fan, J. Sun, Q. Chen, X. Pan, L. Tian, and C. Zuo, "Optimal illumination scheme for isotropic quantitative differential phase contrast microscopy," *Photon. Res.* **7**, 890–904 (2019).
5. Y. Fan, J. Sun, Q. Chen, J. Zhang, and C. Zuo, "Wide-field anti-aliased quantitative differential phase contrast microscopy," *Opt. Express* **26**, 25129–25146 (2018).
6. L. Tian, J. Wang, and L. Waller, "3D differential phase-contrast microscopy with computational illumination using an LED array," *Opt. Lett.* **39**, 1326–1329 (2014).
7. H.-H. Chen, Y.-Z. Lin, and Y. Luo, "Isotropic differential phase contrast microscopy for quantitative phase bio-imaging," *J. Biophotonics* **11**, e201700364 (2018).
8. D. Carpentras, T. Laforest, M. Künzi, and C. Moser, "Effect of back-scattering in phase contrast imaging of the retina," *Opt. Express* **26**, 6785–6795 (2018).
9. T. Laforest, M. Künzi, L. Kowalczyk, D. Carpentras, F. Behar-Cohen, and C. Moser, "Transscleral optical phase imaging of the human retina," *Nat. Photonics* **14**, 439–445 (2020).
10. P. Casteleiro Costa, P. Ledwig, A. Bergquist, J. Kurtzberg, and F. E. Robles, "Noninvasive white blood cell quantification in umbilical cord blood collection bags with quantitative oblique back-illumination microscopy," *Transfusion* **60**, 588–597 (2020).
11. W. Lee, J. H. Choi, S. Ryu, D. Jung, J. Song, J. S. Lee, and C. Joo, "Color-coded LED microscopy for quantitative phase imaging: implementation and application to sperm motility analysis," *Methods* **136**, 66–74 (2018).
12. P. Ledwig and F. E. Robles, "Epi-mode tomographic quantitative phase imaging in thick scattering samples," *Biomed. Opt. Express* **10**, 3605–3621 (2019).
13. C. Bonati, T. Laforest, M. Kunzi, and C. Moser, "Phase sensitivity in differential phase contrast microscopy: limits and strategies to improve it," *Opt. Express* **28**, 33767–33783 (2020).
14. S. Batabyal, S. Satpathy, L. Bui, Y. T. Kim, S. Mohanty, R. Bachoo, and D. P. Dave, "Label-free optical detection of action potential in mammalian neurons," *Biomed. Opt. Express* **8**, 3700–3713 (2017).
15. T. Ling, K. C. Boyle, G. Goetz, P. Zhou, Y. Quan, F. S. Alfonso, T. W. Huang, and D. Palanker, "Full-field interferometric imaging of propagating action potentials," *Light Sci. Appl.* **7**, 107 (2018).
16. T. Ling, K. C. Boyle, V. Zuckerman, T. Flores, C. Ramakrishnan, K. Deisseroth, and D. Palanker, "High-speed interferometric imaging reveals dynamics of neuronal deformation during the action potential," *Proc. Natl. Acad. Sci. USA* **117**, 10278–10285 (2020).
17. S. Oh, C. Fang-Yen, W. Choi, Z. Yaqoob, D. Fu, Y. Park, R. R. Dassari, and M. S. Feld, "Label-free imaging of membrane potential using membrane electromotility," *Biophys. J.* **103**, 11–18 (2012).
18. G. Goetz, T. Ling, T. Gupta, S. Kang, J. Wang, P. D. Gregory, B. H. Park, and D. Palanker, "Interferometric mapping of material properties using thermal perturbation," *Proc. Natl. Acad. Sci. USA* **115**, E2499–E2508 (2018).
19. B. Bhaduri, C. Edwards, H. Pham, R. Zhou, T. H. Nguyen, L. L. Goddard, and G. Popescu, "Diffraction phase microscopy: principles and applications in materials and life sciences," *Adv. Opt. Photonics* **6**, 57–119 (2014).
20. S. Beer and P. Seitz, "Real-time tomographic imaging without X-rays: a smart pixel array with massively parallel signal processing for real-time optical coherence tomography performing close to the physical limits," in *PhD Research in Microelectronics and Electronics Proceedings* (2005), pp. 335–338.
21. S. Beer, S. Waldis, and P. Seitz, "Video-rate optical coherence tomography imaging with smart pixels," *Proc. SPIE* **5140**, 69–76 (2003).
22. S. Beer, P. Zeller, N. Blanc, F. Lustenberger, and P. Seitz, "Smart pixels for real-time optical coherence tomography," *Proc. SPIE* **5302**, 21–32 (2004).
23. B. Buttgen and P. Seitz, "Robust optical time-of-flight range imaging based on smart pixel structures," *IEEE Trans. Circuits Syst. I*, **55**, 1512–1525 (2008).
24. F. Timischl, "The contrast-to-noise ratio for image quality evaluation in scanning electron microscopy," *Scanning* **37**, 54–62 (2015).
25. H. Jiang, N. Lu, and L. Yao, "A high-fidelity haze removal method based on HOT for visible remote sensing images," *Remote Sens.* **8**, 844 (2016).
26. P. Hosseini, R. J. Zhou, Y. H. Kim, C. Peres, A. Diaspro, C. F. Kuang, Z. Yaqoob, and P. T. C. So, "Pushing phase and amplitude sensitivity limits in interferometric microscopy," *Opt. Lett.* **41**, 1656–1659 (2016).
27. L. Azzari and A. Foi, "Gaussian-Cauchy mixture modeling for robust signal-dependent noise estimation," in *IEEE International Conference on Acoustics, Speech and Signal Processing (ICASSP)* (2014), pp. 5357–5361.
28. A. Foi, M. Trimeche, V. Katkovnik, and K. Egiazarian, "Practical Poissonian-Gaussian noise modeling and fitting for single-image raw-data," *IEEE Trans. Image Process.* **17**, 1737–1754 (2008).
29. F. M. Dickey, M. Zimmermann, D. L. Shealy, N. Lindlein, R. Voelkel, and K. J. Weible, "Microlens laser beam homogenizer: from theory to application," *Proc. SPIE* **6663**, 666302 (2007).
30. D. P. O'Leary, "Near-optimal parameters for Tikhonov and other regularization methods," *SIAM J. Sci. Comput.* **23**, 1161–1171 (2001).
31. W. Lee, D. Jung, S. Ryu, and C. Joo, "Single-exposure quantitative phase imaging in color-coded LED microscopy," *Opt. Express* **25**, 8398–8411 (2017).
32. H. Lu, J. Chung, X. Ou, and C. Yang, "Quantitative phase imaging and complex field reconstruction by pupil modulation differential phase contrast," *Opt. Express* **24**, 25345–25361 (2016).